*materials*

MDPI

*Article*

# Maghemite ($\gamma$-$Fe_2O_3$) and $\gamma$-$Fe_2O_3$-$TiO_2$ Nanoparticles for Magnetic Hyperthermia Applications: Synthesis, Characterization and Heating Efficiency

**O. M. Lemine [1,*], Nawal Madkhali [1], Marzook Alshammari [2], Saja Algessair [1], Abbasher Gismelseed [3], Lassad El Mir [4], Moktar Hjiri [4,5], Ali A. Yousif [3] and Kheireddine El-Boubbou [6,7]**

1 Department of Physics, College of Sciences, Imam Mohammad Ibn Saud Islamic University (IMISU), Riyadh 11623, Saudi Arabia; NAmadkhali@imamu.edu.sa (N.M.); saja.algessair@imamu.edu.sa (S.A.)
2 The National Center for Laser and Optoelectronics, KACST, 6086, Riyadh 11442, Saudi Arabia; alshammari@kacst.edu.sa
3 Department of Physics, College of Science, Sultan Qaboos University, Code 123, Al Khoud P.O. Box 36, Oman; Abbasher@squ.edu.om (A.G.); ayousif@squ.edu.sa (A.A.Y.)
4 Laboratory of Physics of Materials and Nanomaterials Applied at Environment (LaPhysMNE), Faculty of Sciences of Gabes, University of Gabes, Gabes 6072, Tunisia; elmirlassad@gmail.com (L.E.M.); M.Hjiri@kau.edu.sa (M.H.)
5 Department of Physics, Faculty of Sciences, King Abdulaziz University, Jeddah 21589, Saudi Arabia
6 Department of Basic Sciences, College of Science & Health Professions, King Saud bin Abdulaziz University for Health Sciences (KSAU-HS), King Abdulaziz Medical City, National Guard Health Affairs, Riyadh 11481, Saudi Arabia; elboubboukh@ngha.med.sa
7 King Abdullah International Medical Research Center (KAIMRC), King Abdulaziz Medical City, National Guard Hospital, Riyadh 11426, Saudi Arabia
* Correspondence: mamamin@imamu.edu.sa; Tel.: +966-112586775



**Citation:** Lemine, O.M.; Madkhali, N.; Alshammari, M.; Algessair, S.; Gismelseed, A.; Mir, L.E.; Hjiri, M.; Yousif, A.A.; El-Boubbou, K. Maghemite ($\gamma$-$Fe_2O_3$) and $\gamma$-$Fe_2O_3$-$TiO_2$ Nanoparticles for Magnetic Hyperthermia Applications: Synthesis, Characterization and Heating Efficiency. *Materials* **2021**, *14*, 5691. https://doi.org/10.3390/ma14195691

Academic Editor: Tatyana I. Shabatina

Received: 30 August 2021
Accepted: 26 September 2021
Published: 30 September 2021



**Abstract:** In this report, the heating efficiencies of $\gamma$-$Fe_2O_3$ and hybrid $\gamma$-$Fe_2O_3$-$TiO_2$ nanoparticles NPs under an alternating magnetic field (AMF) have been investigated to evaluate their feasible use in magnetic hyperthermia. The NPs were synthesized by a modified sol-gel method and characterized by different techniques. X-ray diffraction (XRD), Mössbauer spectroscopy and electron microscopy analyses confirmed the maghemite ($\gamma$-$Fe_2O_3$) phase, crystallinity, good uniformity and 10 nm core sizes of the as-synthesized composites. SQUID hysteresis loops showed a non-negligible coercive field and remanence suggesting the ferromagnetic behavior of the particles. Heating efficiency measurements showed that both samples display high heating potentials and reached magnetic hyperthermia (42 °C) in relatively short times with shorter time (~3 min) observed for $\gamma$-$Fe_2O_3$ compared to $\gamma$-$Fe_2O_3$-$TiO_2$. The specific absorption rate (SAR) values calculated for $\gamma$-$Fe_2O_3$ (up to 90 W/g) are higher than that for $\gamma$-$Fe_2O_3$-$TiO_2$ (~40 W/g), confirming better heating efficiency for $\gamma$-$Fe_2O_3$ NPs. The intrinsic loss power (ILP) values of 1.57 $nHm^2/kg$ and 0.64 $nHm^2/kg$ obtained for both nanocomposites are in the range reported for commercial ferrofluids (0.2–3.1 $nHm^2/kg$). Finally, the heating mechanism responsible for NP heat dissipation is explained concluding that both Neel and Brownian relaxations are contributing to heat production. Overall, the obtained high heating efficiencies suggest that the fabricated nanocomposites hold a great potential to be utilized in a wide spectrum of applications, particularly in magnetic photothermal hyperthermia treatments.

**Keywords:** iron oxide nanoparticles; maghemite; $TiO_2$; Sol-Gel synthesis; magnetic hyperthermia; heating efficiency; alternating magnetic field

## 1. Introduction

The unique properties of magnetic iron oxide nanoparticles (NPs) confirmed its use in several applications such as photocatalysis, photonic, magnetic storage and electronic devices to biomedicine and theranostics [1,2]. Among these applications in clinical practice is their utilization in magnetic fluid hyperthermia (MFH) [3]. This is chiefly due to their

excellent intrinsic magnetic properties, ultrasmall nanometer dimensions (5–15 nm) and their ability for dissipating heat using an alternating magnetic field (AMF). In particular, ferrites (mainly magnetite ($Fe_3O_4$) or maghemite ($\gamma$-$Fe_2O_3$)) are very promising materials for MFH and have been effectively utilized for cancer hyperthermia therapy [4–6]. Furthermore, a combination of iron-based nanoprobes with other transition metals (i.e., Ti, Au, Ag) at the nanoscale lead to formation of bifunctional materials which benefits from the unique properties of both components. Consequently, bifunctional iron oxide-based NPs, with both photo and magnetic properties, are expected to exhibit high potentials, particularly in multimodal photothermal therapies [7–9]. There is, therefore, a pressing need to understand the heat generated from such hybrid constructs and to show the influence of the added metal on the overall magnetism and heating properties of iron oxides.

The advantage of $\gamma$-$Fe_2O_3$, the rare form of iron oxides, over other metal doped ferrite NPs is their magnetism and relatively high saturation magnetization. $\gamma$-$Fe_2O_3$ is a spinel ferrite and has almost the same structure as $Fe_3O_4$, but it converts to alpha hematite ($\alpha$-$Fe_2O_3$) at very high temperatures [10–12]. Thus, the impeccable synthetic routes to achieve a series of uniform, size-controlled, highly-magnetic, crystalline and stable $\gamma$-$Fe_2O_3$ NPs remain unambiguously challenging. To date, several different methods have been employed to synthesize iron oxide NPs including non-aqueous and aqueous sol-gel, spray/laser pyrolysis, sonochemical, microemulsion, hydrothermal, chemical precipitation and thermal decomposition [13]. However, preparation of $\gamma$-$Fe_2O_3$ NPs continues to be difficult and often leads to phase transitions and loss of crystallinity during the synthesis [14]. Another important factor relies on employing modest, feasible and cost-effective route to prepare big quantities of NPs on demand. On the other hand, among other oxide semiconductors, $TiO_2$ was the most interesting material due to its high photocatalytic activity, biochemical inertness, strong oxidizing power, relatively low price and long-term chemical and thermal stability against photo and chemical degradation. Therefore, the immobilization of $TiO_2$ onto magnetic ferrite NPs could serve as an excellent material that could be used for wide range of applications (water treatment, disinfection, pollutant degradation and photothermal hyperthermia therapy). Most of the reports on iron oxide-$TiO_2$ nanocomposites, however, focused their studies on the photocatalytic activities and showed that iron oxide NPs enhance the photocatalytic properties of $TiO_2$ [15–20]. Only few research works investigated the heating efficiency of these nanocomposites for possible use in magnetic hyperthermia applications [19,20]. Shariful Islam et al. [19] studied the thermal-photocatalytic cell killing efficiency of $Fe_3O_4$–$TiO_2$. It was found that the cancer cell killing percentage was enhanced by combining an altenating magnetic-field induction and UV–vis photoirradiation in comparison to only bare $Fe_3O_4$ or $TiO_2$. Lu et al. [20] investigated the hyperthermia abilities and photocatalytic activities of porous $\gamma$-$Fe_2O_3$ microspheres decorated with $TiO_2$. They reported a good heating ability of the composites, which make them promising candidate for magnetic hyperthermia applications.

In fact, magnetic hyperthermia using iron oxide NPs is currently boosting as such probes can act as efficient and local nanoheaters through remote activation (i.e., by AMF), which leads to remarkable therapeutic effects. However, their success relies on the precise control of their magnetic properties, sizes, specific absorption rate (SAR) and intrinsic loss power (ILP), as well as tuning parameters such as concentrations and amplitude of the applied magnetic field. The heat dissipated using an AC magnetic field is characteristically known by SAR, which is the amount of heat generated per unit gram of magnetic material and per unit time [21,22]. Previous studies reported that SAR values could be influenced by different parameters, among them, size, structure, magnetic properties, preparation methods, concentration and the frequency and amplitudes of the applied magnetic field [23–27]. De la Presa et al. prepared $\gamma$-$Fe_2O_3$ NPs by the technique called co-precipitation and demonstrated the effect of different parameters on SAR [24]. They found that the critical crystallite size to obtain maximum efficiency of heat was 12 nm. We previously investigated the heating efficiency of different sizes $\gamma$-$Fe_2O_3$ NPs using sol-gel technique [25,26] and we obtained that 14 nm was the best size to acquire preferable heating efficiency. In addition

to the above parameters, the magnetic particle-particle interactions could also affect SAR values. Despite the large number of reports on the effect of variable parameters on SAR, the key factors affecting the heat dissipation is still not very well understood.

Herein, we report a simple process using modified sol-gel strategy to synthesize maghemite and maghemite-$TiO_2$ nanocomposites. We tested whether the presence of $TiO_2$ affect particle-particle magnetic interactions and induce any effects on heating abilities. We then studied the influence of magnetic properties and amplitude of the exercised magnetic field on heating abilities (SAR values) for the acquired particles. Finally, we discussed the plausible heating mechanism responsible for the generation of heat from the obtained NPs. The best we know, there is no report systematically studying different effects on the heating efficiencies of $\gamma$-$Fe_2O_3$ NPs and hybrid $\gamma$-$Fe_2O_3$-$TiO_2$ NPs. These $\gamma$-$Fe_2O_3$@$TiO_2$ nanocomposites, which integrate photo and magnetic properties, have great potential to be used in wide range of applications, particularly in medical photothermal hyperthermia.

## 2. Experimental

### *2.1. Synthesis of Maghemite and Maghemite-$TiO_2$ Nanoparticles*

In the first step, $\gamma$-$Fe_2O_3$ NPs were synthesized by a modified Sol-gel process in supercritical conditions of ethyl alcohol (EtOH) following similar procedure as in our previous work [25]. 5 g of iron (III) acetylacetonate [$C_{15}H_{12}FeO_6$, 99%] obtained from Chemsavers was dissolved in a 30 mL of methanol ($CH_3OH$, 98%) obtained from SIGMA-ALDRICH, under magnetic stirring of 400 rpm at room temperature for 15 min. The solution was then placed in an autoclave and dried under supercritical conditions of of ethanol ($C_2H_6O$, 96%) fabricated by Honeywell. The supercritical conditions of ethanol are $P_c$ = 63.3 bar and Tc = 243 °C. The control of the heating of the autoclave was realised by temperature programmer.

In the second step, $TiO_2$ NPs enriched by $Fe_2O_3$ particles were obtained by dissolving of 6.72 mmol of titanium (IV)-isoproxide ($Ti(iOPr)_4$, 97%, from Chemsavers ) in a mixture of methanol and acetic acid (2 mL/2 mL). After 15 min of magnetic stirring, 50 mg of $Fe_2O_3$ NPs prepared in the first step was added to the solution and introduced in ultrasonic bath for 10 min. The temperature range was varied from ambient to 250 °C. The resulted solution was then introduced in an autoclave and dried in the supercritical condition of ethanol by using 600 mL.

This simple and cost-effective synthesis allowed the production of large quantities of $\gamma$-$Fe_2O_3$ NPs and $\gamma$-$Fe_2O_3$-$TiO_2$ NPs on demand.

### *2.2. Structural Measurements*

Using Bruker D8 Discover diffractometer ($\theta$-$2\theta$) equipped with Cu-K$\alpha$ radiation ($\lambda$ = 1.5406 Å), XRD analyses were made. The average crystallite size, D, of different samples was estimated by Scherrer's formula [28]:

$$D = \frac{K\lambda}{\beta cos\theta} \quad (1)$$

where $\theta$ is the Bragg angle (in degree), $\lambda$ is the incident wavelength (1.5406 Å), $K$ is a constant whose value is approximately 0.9 and $\beta$ (rad) is the full width at half maximum (FWHM) of a diffraction peak. Fourier transform infrared (FTIR) spectra were obtained using a Perkin-Elmer 580B IR spectrometer. The morphology of the samples was studied by means of transmission electron microscope (Type JEOL JSM-200F atomic resolution microscopy operating at 200 kV, Tokyo, Japan).

### *2.3. Magnetic Characterization*

Mössbauer spectra were recorded at ambient temperature (RT = 295 K) and 78 K in standard transmission geometry using a constant acceleration signal spectrometer equipped with a $^{57}$Co source in a rhodium matrix. The data were analyzed using a non-linear least-squares fitting program assuming a Lorentzian distribution. Isomer shifts are presented

in reference to α-Fe. Magnetic characterizations were performed in a Quantum Design MPMS-5S SQUID magnetometer (San Diego, CA, USA). Zero-field-cooled and field-cooled (ZFC-FC) curves were recorded at magnetic field of 100 Oe.

### *2.4. Heating Efficiency*

A commercial system "Nanotherics Magnetherm" was used to carry out the heating efficiency of the samples under alternating current (AC) magnetic field as reported in our previous report [28]. The heat generated by magnetic nanoparticles for magnetic hyperthermia measurement is quantified by the *SAR*, which can be determined by:

$$SAR = \frac{\rho C_w}{Mass_{MNP}} \left( \frac{\Delta T}{\Delta t} \right) \quad (2)$$

where $C_w$ is defined as the specific heat capacity of water (4.185 $J \cdot kg^{-1} \cdot K^{-1}$), the density of the colloid is $\rho$, the concentration of the magnetic nanoparticles in the suspension is called $Mass_{MNP}$ and the heating rate is represented by $\frac{\Delta T}{\Delta t}$. By performing a linear fit of temperature increase versus time at the initial time interval (1 to ~30 s), the slope $\Delta T / \Delta t$ is obtained. The influence of concentration (10 and 20 mg/mL) has been studied. To show the effect of different amplitudes (40, 90 and 130) of the magnetic field and 170 Oe at 332.8 kHz on the heating ability of the as-prepared NPs, one has selected a concentration of 10 mg/mL. All the samples are dispersed in deionized water

## 3. Results and Discussion

### *3.1. Structural Properties*

XRD spectra of the obtained nanocomposites are shown in Figure 1. As can be seen in Figure 1a, XRD patterns of $Fe_2O_3$ NPs indicated the presence of diffraction peaks which correspond to spinel structure, which could be indexed on the basis of γ-$Fe_2O_3$ with space group P4132 (JCPDS No. 39-1346). No additional peaks have been observed suggesting that our synthetic method lead to the formation of a pure phase without any impurities that remain from the unreacted precursors. XRD patterns of γ-$Fe_2O_3$-$TiO_2$ nanocomposite (Figure 1b) are similar to patterns obtained for γ-$Fe_2O_3$ but new peaks appear at $2\theta$ = 25.3°, 37.86°, 48.2°, 54.1°, 55.2° are attributed to anatase-$TiO_2$ [29], while the peaks located at 2θ = 27.57°, 41.02°, 54.3°, 68.96° are due to the rutile $TiO_2$ [30]. We can conclude from XRD results the successful formation of γ-$Fe_2O_3$-$TiO_2$ nanocomposite and that the addition of $TiO_2$ did not induce any significant phase changes on the γ-$Fe_2O_3$ NPs. It is important also to note that the peaks for both samples are very broad indicating the formation of very fine particles. The average crystallite size obtained by using the Debye-Scherrer formula confirms this result. The average crystallite size estimated for γ-$Fe_2O_3$ was 8.5 nm. This value increased to 10 nm after adding $TiO_2$ which has an average crystallite size of 16.5 nm and 22 nm for anatase and rutile phases, respectively.

FTIR was then extended to confirm the presence of $Fe_2O_3$ and $Fe_2O_3$-$TiO_2$ (Figure 2). FTIR spectrum of γ-$Fe_2O_3$ showed a broad band at 3434 $cm^{-1}$and 1630 $cm^{-1}$ attributed to the O-H stretching and bending vibrations of surface hydroxyl, respectively. Another peak at 2927 $cm^{-1}$ may corresponds to C-H groups stretching vibration. The band at 1420 $cm^{-1}$ is attributed to the C-O stretching vibration, while the bands at 635 $cm^{-1}$ and 583 $cm^{-1}$ are associated with the Fe-O vibrational modes confirming the presence of iron oxide. The γ-$Fe_2O_3$-$TiO_2$ shows a similar FTIR spectrum to that of γ-$Fe_2O_3$ with wide absorption band at 420–825 $cm^{-1}$. This wide absorption band is attributed to Ti-O vibrations [20].

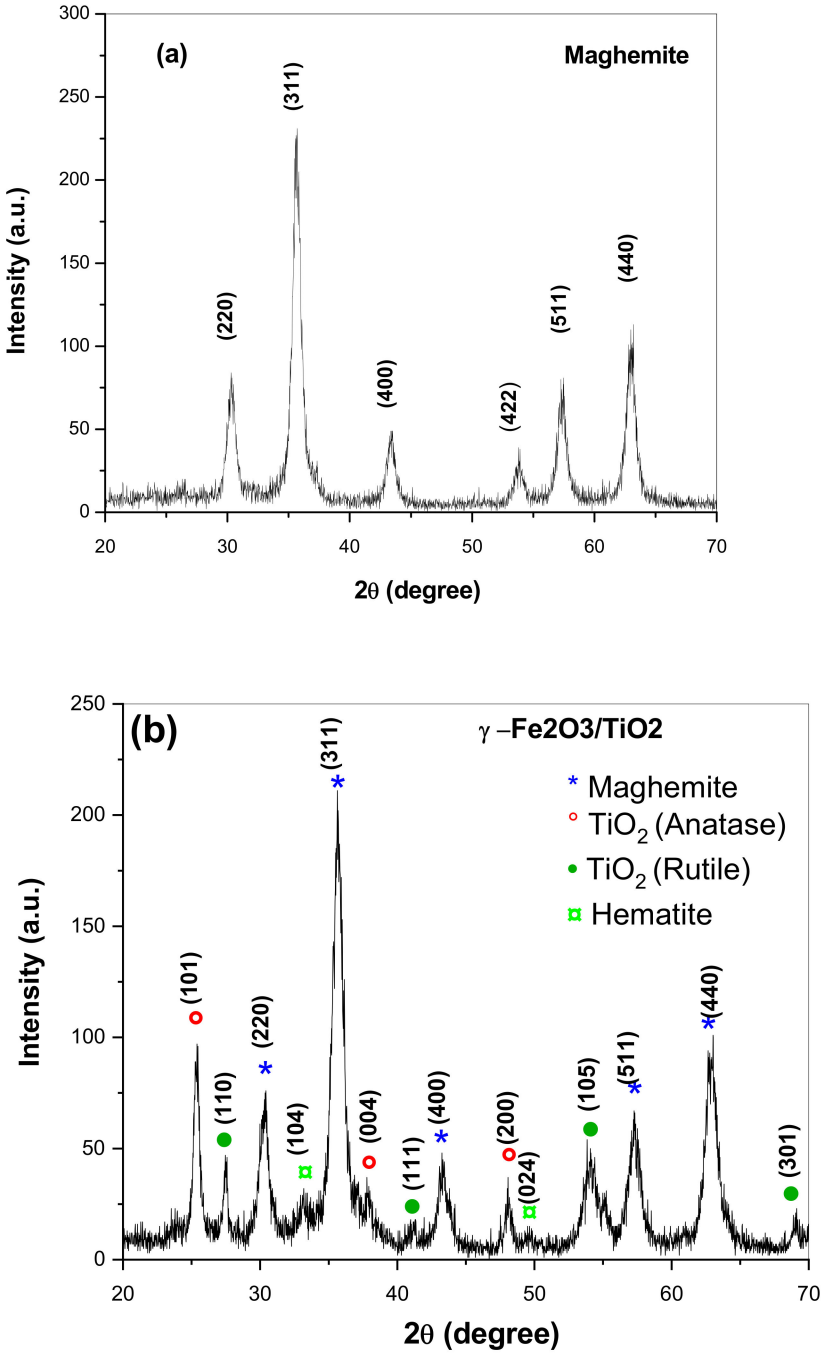


**Figure 1.** XRD patterns of (**a**) γ-$Fe_2O_3$ and (**b**) γ-$Fe_2O_3$-$TiO_2$ nanocomposites.

To better analyze the size and morphology of the obtained nanocomposites, transmission electron microscopy (TEM) was conducted. Figure 3a,b shows TEM images of γ-$Fe_2O_3$ and γ-$Fe_2O_3$-$TiO_2$ nanocomposites, respectively. The images clearly indicate the quasi-cubic morphology of the samples with average core sizes of γ-$Fe_2O_3$ equal to 8.5 nm and slightly increases for γ-$Fe_2O_3$-$TiO_2$ to 11 nm. The particle size distribution associated with the TEM images confirm the good uniformity of the as-synthesized NPs (Figure 3c,d).

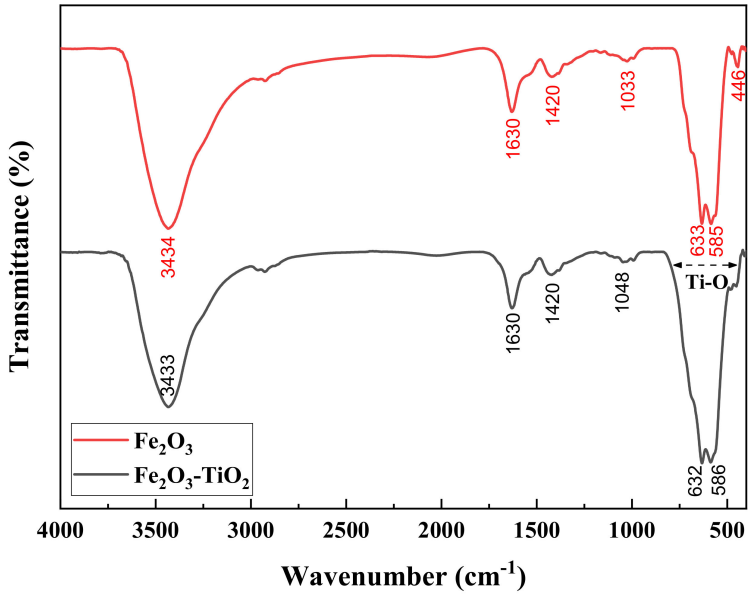


**Figure 2.** FTIR spectra of γ-$Fe_2O_3$ (up) and γ-$Fe_2O_3$-$TiO_2$ (down) NPs.

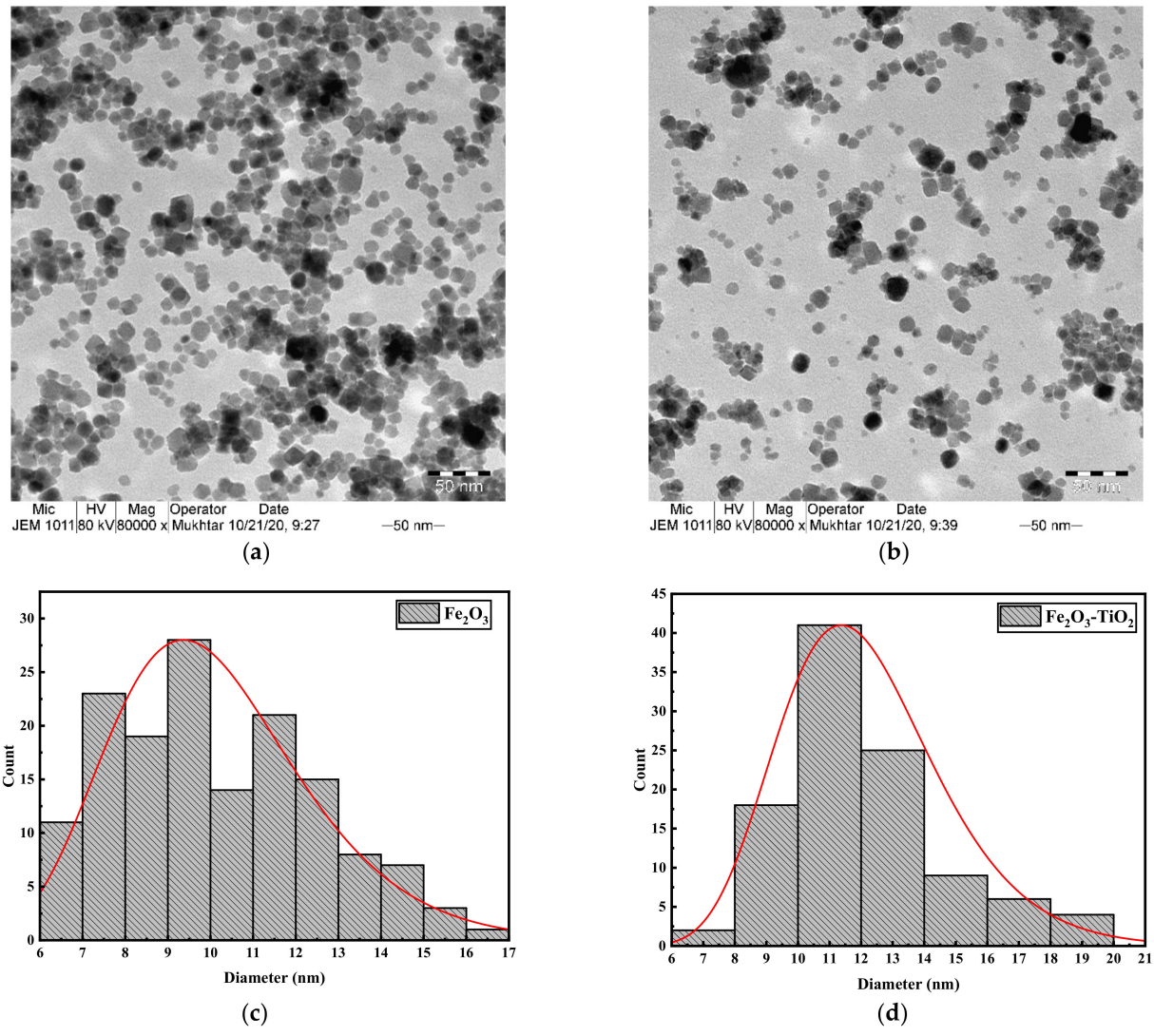


**Figure 3.** TEM photographs (**a**,**b**) particles size distribution (**c**,**d**) γ-$Fe_2O_3$ and γ-$Fe_2O_3$-$TiO_2$ nanocomposite respectively.

### *3.2. Magnetic Characterization*

#### 3.2.1. SQUID Measurements

Hysteresis loops and ZFC-FC curves for γ-$Fe_2O_3$ and γ-$Fe_2O_3$-$TiO_2$ NPs are shown in Figure 4. The saturation magnetization (*Ms*), remanance (*Mr*), remnant to saturation magnetization ratio (*Mr*/*Ms*) and coercive field (*Hc*) values are presented in Table 1. It can be seen that the samples exhibit a non-negligible coercive field at room temperature, indicating that the particles do not behave as superparamagnetic (Figure 4a,b). The saturation magnetization at room temperature estimated for γ-$Fe_2O_3$ (*Ms* = 84.5 emu/g) is higher than the standard value reported for bulk maghemite γ-$Fe_2O_3$ ($M_s$ = 74 emu/g) but comparable to those reported in previous studies [24]. This is because of the spin disorder in surface that can be aligned readily in the applied magnetic field direction [31]. It might be also due to the presence of magnetite phase which has high magnetization, but XRD and Mossbauer results (discussed later) confirm the absence of this phase in the sample. The observed decrease of saturation of γ-$Fe_2O_3$-$TiO_2$ NPs (*Ms* = 58.77 emu/g) is due to the non-magnetic nature of $TiO_2$. Previous studies reported similar behavior of saturation after coating magnetite and maghemite with $TiO_2$ [18,32]. To further understand the magnetic behavior of the samples, magnetization as a function of temperature using the zero-field-cooled and field-cooled (ZFC-FC) were performed (Figure 4c,d). The ZFC-FC curves indicate that blocking temperature ($T_B$) for γ-$Fe_2O_3$ NPs is above room temperature, while $T_B$ is around 240K for γ-$Fe_2O_3$-$TiO_2$ NPs.

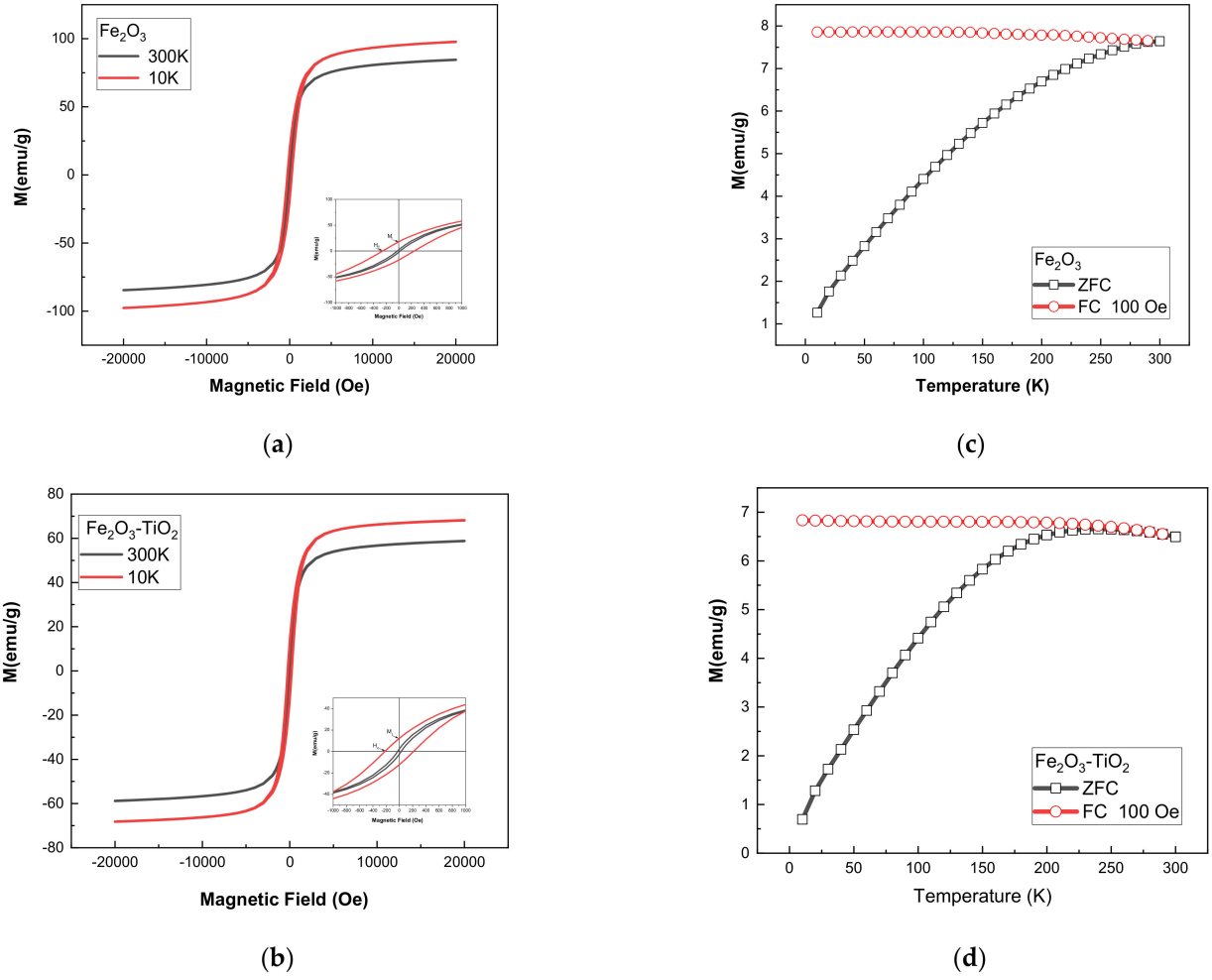


**Figure 4.** Hysteresis loops of (**a**) γ-$Fe_2O_3$ and (**b**) γ-$Fe_2O_3$-$TiO_2$ nanocomposites. ZFC/FC curves of (**c**) γ-$Fe_2O_3$ and (**d**) γ-$Fe_2O_3$-$TiO_2$.

**Table 1.** Magnetic parameters deduced from hysteresis loops and anisotropy constant ($K_{eff}$) for γ-$Fe_2O_3$ and γ-$Fe_2O_3$-$TiO_2$.

| Samples | $M_s$ (emu/g) | | $M_r$ (emu/g) | | $M_r/M_s$ | | $H_c$ (Oe) | | $K_{eff}$ (erg/cm$^3$) | | D (nm) |
|---|---|---|---|---|---|---|---|---|---|---|---|
| | 10 K | 300 K | 10 K | 300 K | 10 K | 300 K | 10 K | 300 K | 10 K | 300 K | |
| $Fe_2O_3$ | 97.76 | 84.55 | 17.51 | 2.69 | 0.179 | 0.032 | 252.17 | 23.26 | $6.44 \times 10^3$ | $5.68 \times 10^4$ | 8.5 |
| $Fe_2O_3$-$TiO_2$ | 68.11 | 58.77 | 12.25 | 3.11 | 0.18 | 0.053 | 217.51 | 27 | $3.51 \times 10^3$ | $3.43 \times 10^3$ | 11 |

The coercive field $H_C$ increases with decreasing temperature for both samples due perhaps to the blocking of magnetic moments. The behavior of $H_C$ at room temperature for the two samples can be analyzed in term of size. It can be seen that coercivity at room temperature increase slightly for γ-$Fe_2O_3$-$TiO_2$ nanocomposite ($H_C$ = 27 Oe) compared to γ-$Fe_2O_3$ ($H_C$ = 23 Oe). This behavior can be understood on the basis of model describing the magnetic behavior in the monodomain regime; where coercivity follow the relation [24,33]:

$$H_C = \left(\frac{2K_{eff}}{\mu_0 M_s}\right)\left[1 - \frac{25K_B T}{K_{eff} V}\right] \quad (3)$$

where $K_{eff}$ is effective anisotropy constant, $M_S$ is the saturation and $V$ is the volume of the nanoparticles. It can be seen from the relation (3) that the coercive field depends on saturation, the volume and effective anisotropy constant. All these parameters are size dependent and that can explain the decrease of the coercivity with decreasing size.

Using the law of approach to saturation (LAS), we attempt to calculate the anisotropy constant $K_{eff}$ which characterize the magnetization close to the saturation as below [34,35]:

$$M(H) = M_s\left(1 - \frac{b}{H^2}\right) \quad (4)$$

where $b$ is a parameter used to determine $K_{eff}$ by using the following equation [25]:

$$K_{eff} = \mu_0 M_s \sqrt{\frac{15b}{4}} \quad (5)$$

The calculated value of $K_{eff}$ for both samples at 10 K and 300 K are summarized in Table 1. As can be seen, the effective anisotropy constant obtained for γ-$Fe_2O_3$ NPs at room temperature ($K_{eff} = 5.68 \times 10^4$ erg/cm$^3$) is close to that reported for bulk γ-$Fe_2O_3$ ($K_{eff} = 4.7 \times 10^4$ erg/cm$^3$) [36].

#### 3.2.2. Mössbauer Spectroscopy

We indexed the phase of the obtained NPs as γ-$Fe_2O_3$ from XRD, but it could be also indexed as $Fe_3O_4$ given that XRD patterns of γ-$Fe_2O_3$ and $Fe_3O_4$ are almost the same. In order to differentiate between the two phases (γ-$Fe_2O_3$ and $Fe_3O_4$) and to confirm that the obtained phase is γ-$Fe_2O_3$, Mössbauer spectroscopy studies were carried out. It is well known that the hyperfine parameters such as isomeric shift and hyperfine field of both Fe-oxides are different. The Mössbauer spectra of the two samples at 78 K and 295 K are shown in Figure 5a and as can be observed, all the spectra show well-defined magnetic sextet pattern. The best fit was obtained by considering two dominating sextets and one small magnetic component A, B and C, respectively, as shown in Figure 5b. As can be seen from Table 2, the isomeric shift values of the main components A (0.40 mm/s) and B (0.43 mm/s) of $Fe_2O_3$ at 78 K are typical of ferric ($Fe^{3+}$) iron [37]. In addition to the isomer shift values, the hyperfine field and quadrupole shifts of both components are the typical characteristics of $Fe^{3+}$ ions in maghemite γ-$Fe_2O_3$ nanoparticles [38]. Furthermore, the hyperfine parameters of the third component C is also attributed to the $Fe^{3+}$ ions. It is important to highlight the absence of ferrous ($Fe^{+2}$), which is characteristic of magnetite ($Fe_3O_4$). Thus, it can be concluded that the synthesized NPs are indexed as γ-$Fe_2O_3$ with

space group P4132 (JCPDS No. 39-1346). The A and B components are attributed to the tetrahedral and octahedral sites of maghemite, respectively, while the third component C is attributed to the iron ions in the surface layer. The spectrum of $Fe_2O_3$-$TiO_2$ at 78 K was fitted with same components and no changes are observed except slight decreases in the hyperfine field values due to the effect of $TiO_2$, which is non-magnetic. This is in agreement with magnetization measurement that clearly shows a decrease of $Fe_2O_3$-$TiO_2$ saturation.

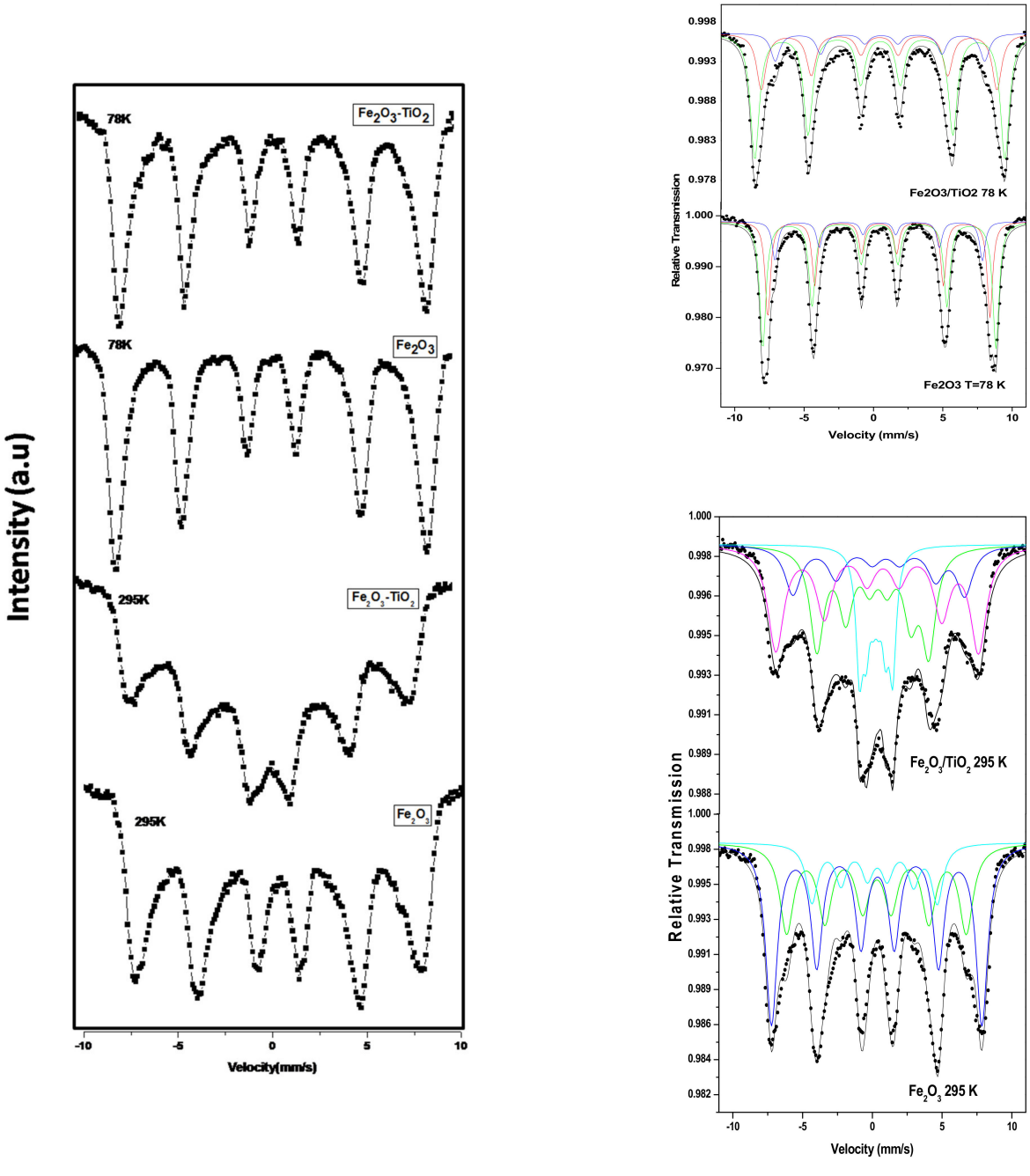


**Figure 5.** (**a**) The $^{57}$Fe Mössbauer spectra of γ-$Fe_2O_3$ and γ-$Fe_2O_3$-$TiO_2$ nanocomposite at 78 and 295 K; (**b**) The calculated spectrum components for both samples corresponding to the tetrahedral (A), octahedral (B) sites of $Fe^{3+}$ ions and iron ions at the surface of the NPs (C).

**Table 2.** Hyperfine parameters deuced from the Mossbauer spectra at 78 and 295 K.

| Samples | Component | Isomer Shifts δ ± (0.01) mm/s | | Quadrupole Shifts ε ± (0.002) mm/s | | Magnetic Hyperfine Field $B_{hf}$ (±0.1) T | | Area A (±1) % | |
|---|---|---|---|---|---|---|---|---|---|
| | | 78 K | 295 K | 78 K | 295 K | 78 K | 295 K | 78 K | 295 K |
| $Fe_2O_3$ | A | 0.40 | 0.31 | −0.007 | −0.021 | 49.7 | 40.0 | 34 | 33 |
| | B | 0.43 | 0.34 | −0.004 | −0.029 | 52.1 | 46.7 | 52 | 51 |
| | C | 0.40 | 0.26 | −0.024 | −0.078 | 46.4 | 27.8 | 14 | 16 |
| $Fe_2O_3/TiO_2$ | A | 0.37 | 0.70 | −0.013 | −0.253 | 47.9 | 38.2 | 32 | 17 |
| | B | 0.43 | 0.54 | −0.020 | −0.211 | 50.9 | 45.1 | 55 | 36 |
| | C | 0.46 | 0.21 | −0.045 | −0.191 | 42.6 | 24.9 | 13 | 30 |
| | D | – | 0.24 | – | −0.009 | – | 7.4 | – | 17 |

The Mössbauer spectra for both samples show well-defined magnetic sextet pattern, but the lines become broadened (Figure 5), indicating that the samples conserved their magnetic order remain. This is in agreement with SQUID measurements, which indicated that both samples are ferromagnetic at room temperature. The phase is confirmed again by fitting the spectra with the same components corresponding to $Fe^{3+}$ ions in the tetrahedral, octahedral and in the surface layer. For γ-$Fe_2O_3$-$TiO_2$ sample, the best fit was obtained by adding paramagnetic doublet component D (Table 2), which is attributed to the transition of some part of NPs from magnetic ordering to a paramagnetic state (Figure 6b). This paramagnetic component is due to part of the NPs, where their blocking temperature $T_B$ is below 295 K. ZFC/FC measurements corroborated this hypothesis and showed that γ-$Fe_2O_3$-$TiO_2$ sample has $T_B$ around 240 K, while $T_B$ for γ-$Fe_2O_3$ is above room temperature. In summary, the Mössbauer results indicated that the phase is maghemite and that both samples are ferrimagnetic at room temperature, which is in agreement with magnetic measurements.

### *3.3. Heating Efficiency Measurements*

#### 3.3.1. SAR as Function of Concentration

The heating efficiencies of γ-$Fe_2O_3$ and γ-$Fe_2O_3$-$TiO_2$ nanocomposites dispersed in deionized water at different concentrations under AMF with frequency and amplitudes that satisfy the magnetic hyperthermia safety condition ($Hxf \leq 5 \times 10^9 A/m.s$) [24] were conducted (Figure 6). The main heating parameters obtained from the temperature rise are summarized in Table 3. As can be seen in Figure 6a,b, all the samples show high heating ability and reach magnetic hyperthermia temperature (42 °C) in short time. For instance, γ-$Fe_2O_3$ reached magnetic hyperthermia temperature in only 3 min, while γ-$Fe_2O_3$-$TiO_2$ took around 4.5 min to reach the same temperature at the same concentration. As expected, the rise in temperature decreases with decreasing the concentration for both samples. While 20 mg/mL sample of γ-$Fe_2O_3$ could reach high temperatures up to 73 °C in 15 min, temperature up to 62 °C was achieved for 10 mg/mL concentration of the same sample. This increase can be explained by the additional amount of magnetic nanostructure, which is generally the main source of heat dissipation. The calculated values of SAR as function of concentration are shown in Figure 6c. It can be seen that SAR values of γ-$Fe_2O_3$ are higher than that obtained for γ-$Fe_2O_3$-$TiO_2$ nanocomposites but both samples have considerable SAR values. As reported by previous reports, interparticles dipolar interaction increases with increasing concentration of NPs and that could induce such effect on the heating [22,39,40]. Abbasi et al. [39] claimed that increase of dipolar interaction with enhancing concentration has a considerable influence on the Neel relaxation time (which will be discussed later).

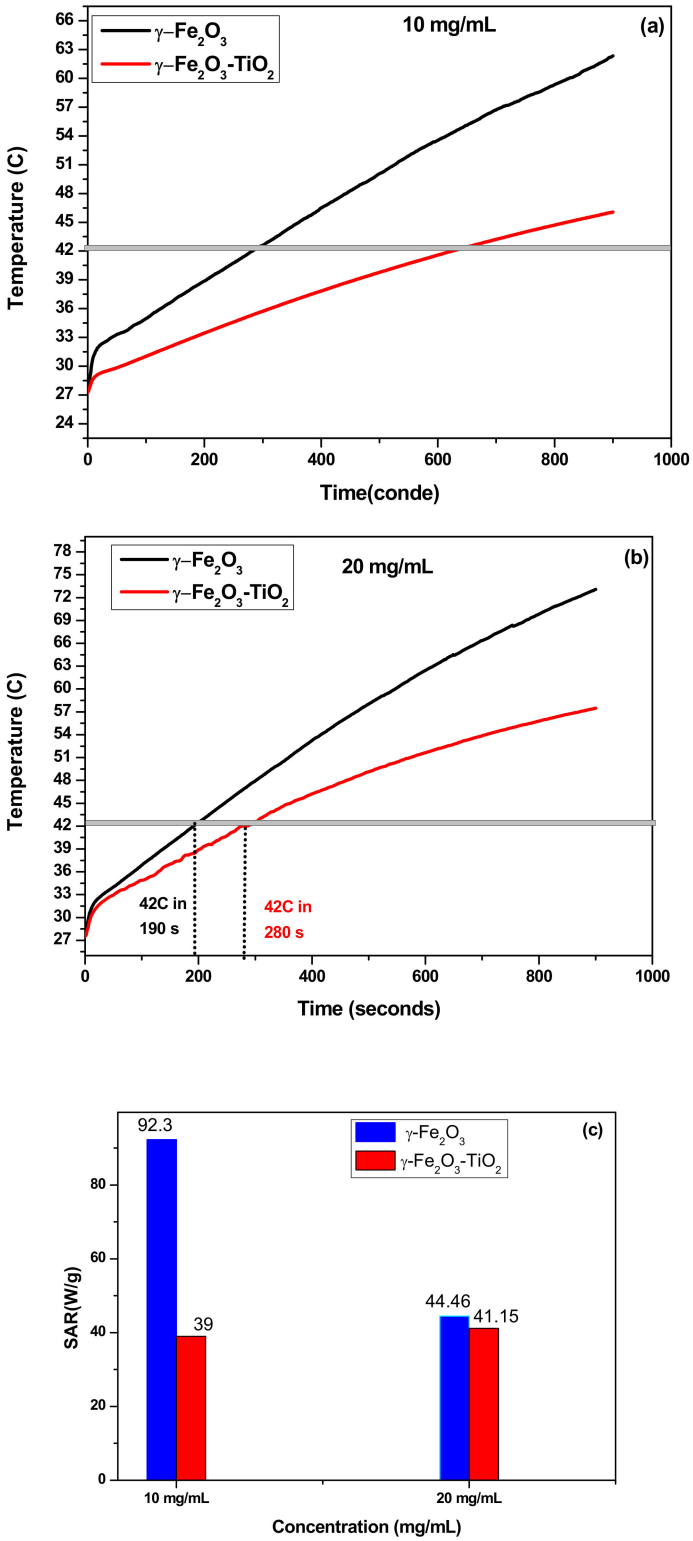


**Figure 6.** Temperature increases at $H_0$ = 170 Oe and $f$ = 332.8 kHz for γ-$Fe_2O_3$ and (**b**) γ-$Fe_2O_3$-$TiO_2$ nanocomposite: (**a**) 10 mg/mL, (**b**) 20 mg/mL and (**c**) SAR values as function of concentration.

**Table 3.** Heating characteristics at $H_0$ = 170Oe and f = 332.8 kHz.

| ILP (nH $m^2$/kg) | SAR (W/g) | Time Needed to Reach Hyperthermia Temperature 42 °C (min) | Maximum Temperature (°C) | Concentration | Samples |
|---|---|---|---|---|---|
| 1.57 | 92.3 | 4.8 | 62 | 10 mg/mL | $\gamma$-$Fe_2O_3$ |
| 0.64 | 39 | 10.5 | 46 | | $\gamma$-$Fe_2O_3$-$TiO_2$ |
| 0.73 | 44.46 | 3 | 73 | 20 mg/mL | $\gamma$-$Fe_2O_3$ |
| 0.67 | 41.15 | 4.6 | 57.5 | | $\gamma$-$Fe_2O_3$-$TiO_2$ |

3.3.2. SAR as Function of Field Amplitude

Figure 7a,b shows the temperature rise of the samples with concentrations of 10 mg/mL in frequency of 332.8 kHz and for different strength of AC magnetic field. When the field amplitude increases from 90 Oe to 170 Oe and as expected, an increase of the temperature is observed (Figure 7c), indicating that the heating efficiency of the NPs can be tuned by changing the field amplitude. As can be observed also in Figure 8a, SAR increases with increasing field amplitude and reached their higher values at field amplitude of 170 Oe for both samples. The same trend of SAR with the field amplitude was reported for many NP systems [22,24,25]. Furthermore, we investigated that the linear response theory (LRT) was valid for the two samples. In this model, *SAR* varies linearly as a function of square of field amplitude and given as below [24]:

$$SAR = cfH^2 \quad (6)$$

where $c$ is a constant, $f$ is the frequency and $H$ is amplitude of the field.

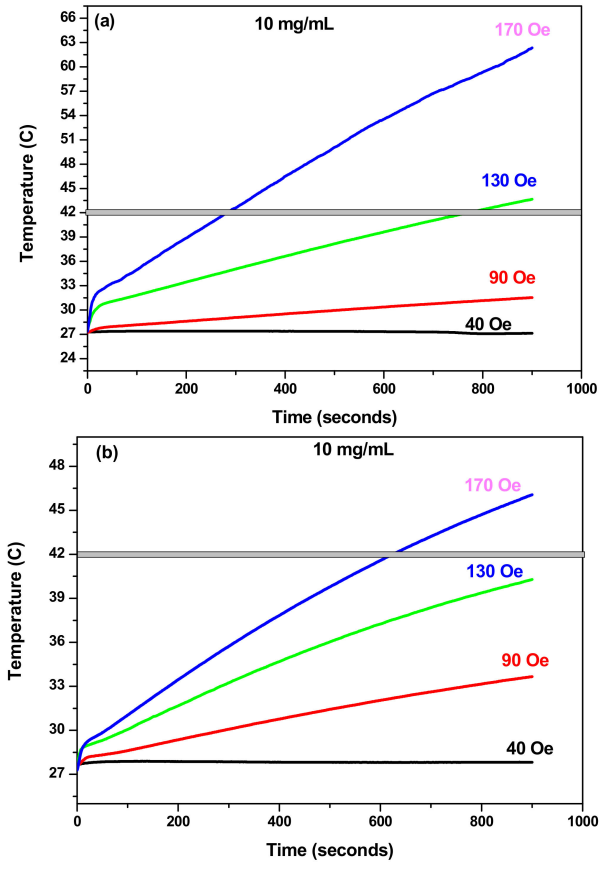


**Figure 7.** *Cont.*

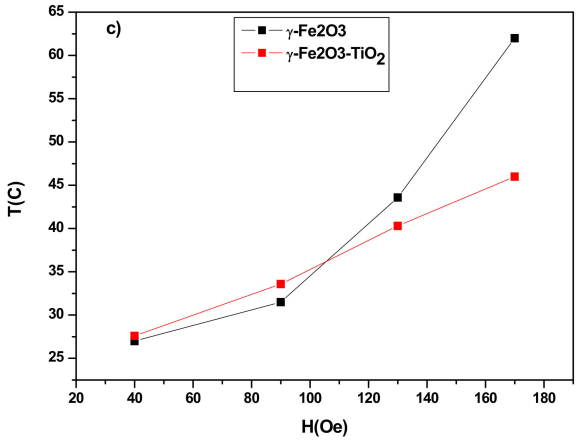


**Figure 7.** Temperature increases at $f$ = 332.8 kHz and different AC magnetic field of (**a**) γ-$Fe_2O_3$, (**b**) γ-$Fe_2O_3$-$TiO_2$ and (**c**) Temperature *vs* field amplitude.

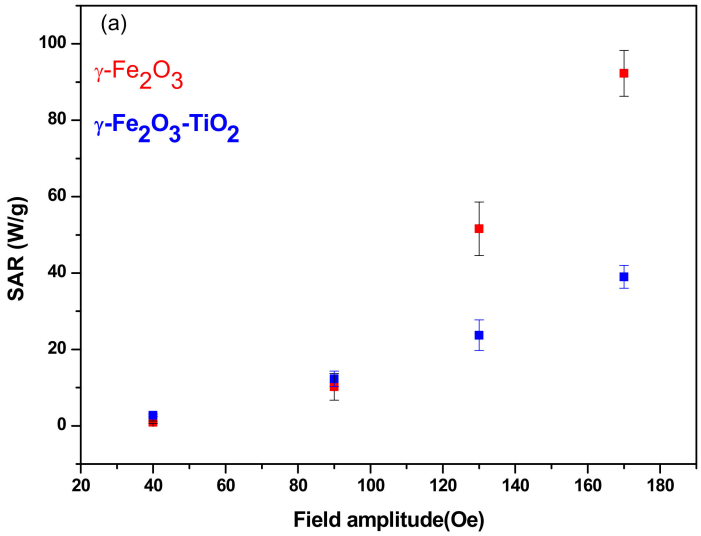


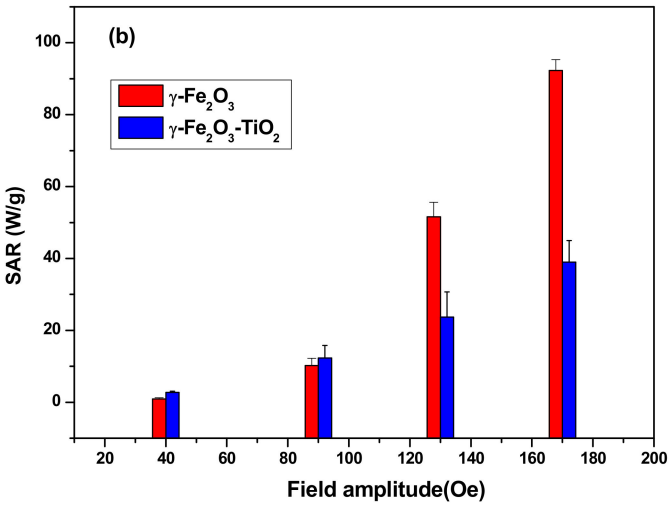


**Figure 8.** (**a**) SAR vs. field amplitude for both samples and (**b**) LRT model showing the evolution of SAR with square of field amplitude.

Figure 8b shows that field amplitude dependence of experimental SARs has a quadratic behavior as expected by the LRT model. The coefficient of determination $R^2$, which should be near 1 for better fit is around 0.998 for both samples and this affirms the high fit accuracy.

#### 3.3.3. Comparison of Heating Ability

Both samples reached magnetic hyperthermia (42 °C) in a relatively short time but the time needed to reach this temperature is shorter in the case of γ-$Fe_2O_3$ compared to γ-$Fe_2O_3$-$TiO_2$ nanocomposites. Furthermore, the SAR values achieved for γ-$Fe_2O_3$ are higher than that obtained for γ-$Fe_2O_3$-$TiO_2$, indicating better heating for γ-$Fe_2O_3$ NPs. This high heating efficiency could be explained mainly by the high saturation of γ-$Fe_2O_3$ NPs (*Ms* = 84.55 emu/g) compared to 58.77 emu/g obtained for γ-$Fe_2O_3$-$TiO_2$. Other parameters such as size of NPs and the effective anisotropy constant ($K_{eff}$) can also affect SAR. However, the effect of size can be neglected due to almost comparable sizes obtained from TEM measurements, while $K_{eff}$ of γ-$Fe_2O_3$ ($5.68 \times 10^4$ erg/cm$^3$) is about 16-fold larger than γ-$Fe_2O_3$-$TiO_2$ nanocomposite value ($3.43 \times 10^3$ erg/cm$^3$).

The comparison of the heating ability of our NPs with other systems through the SAR values is depicted in Table 4. However, this comparison of SAR values does not give much information on the heating efficiency given that each study has its own experimental conditions such as concentration, magnetic properties, field amplitude, frequency etc.

**Table 4.** Comparison of ILP values for different magnetic NPs.

| Magnetic Nanoparticles | Synthesis Method | Frequency (kHz) | Field (Oe) | Medium | ILP (nHm$^2$/kg) | Ref |
|---|---|---|---|---|---|---|
| γ-$Fe_2O_3$ | Modified Sol-gel | 332.8 | 170 | distilled water | 1.57 | This work |
| γ-$Fe_2O_3$ | Modified Sol-gel | 523 | 100 | distilled water | 1.3 | [25] |
| γ-$Fe_2O_3$ -$TiO_2$ | Modified Sol-gel | 332.8 | 170 | distilled water | 0.64 | This work |
| γ-$Fe_2O_3$@$TiO_2$ | Hydrothermal | 55 | 86.7 | Physiological saline | – | [20] |
| $Fe_2O_3$ | Hydrothermal | 200 | 251.3 | distilled water | 1.12 | [40] |
| $Zn_{0.1}Fe_{0.9}Fe_2O_4$ | coprecipitation method | 339 | 92 | distilled water | 5.4 | [41] |

To allow a logic comparison of the heating efficiency, we used the intrinsic loss power (ILP), which is given by [38]:

$$ILP = SAR/fH_0^2 \quad (7)$$

where $f$ is the frequency and $H_0$ is magnetic field.

It can be seen from Table 3 that ILP values for 10 mg/mL sample of γ-$Fe_2O_3$ (1.57 nHm$^2$/kg) is larger than that achieved for the same concentration of γ-$Fe_2O_3$-$TiO_2$ (0.64 nHm$^2$/kg) showing again the high heating efficiency of γ-$Fe_2O_3$ compared to γ-$Fe_2O_3$-$TiO_2$ nanocomposites. However, the ILP values for both samples are in the range reported for commercial ferrofluids (0.2–3.1 nHm$^2$/kg) [42].

#### 3.3.4. Mechanism of Heating

Heat dissipation from magnetic nanoparticles under AC magnetic field is caused by three major mechanisms, namely: Hysteresis loss; Brownian relaxation and Néel relaxation as discussed in our previous report [22,25]. We and others [41,43] believe that all the three mechanisms are collaboratively effective in the heat generation. However, some aspects are more dominant over the others as discussed below.

Generally, hysteresis losses are in proportion with the area (A) of the hysteresis loop. As can be observed from M-H curves (Figure 4), both samples present a minor hysteresis loop area due to the low values of coercivity and remenance. It is therefore reasonable to deduce that the contribution of hysteresis loss in the heat dissipated by the samples can be neglected.

In Néel relaxation, the magnetic moment of NPs suspended in fluid can relax after magnetic field removal and relaxation time is given by:

$$\tau_N = \tau_0 e^{K_{eff} V / k_B T} \tag{8}$$

where $\tau_0 = 10^{-9}$ s, V the particle volume, $K_{eff}$ magnetic anisotropy constant, $k_B$ the Boltzmann constant and $T$ the absolute temperature.

The entire nanoparticles can rotate through Brownian relaxation during time $\tau_B$:

$$\tau_B = \frac{3\eta V_h}{k_B T} \tag{9}$$

where $\eta$ is the viscosity of the fluid and $V_h$ the particle volume.

It can be seen that Néel relaxation time depends exponentially on volume and magnetic anisotropy whereas the Brownian relaxation varies linearly with the volume and the media viscosity.

In most cases, the combination of the two mechanisms is more suitable, but the quick relaxation mechanism is prevalent and an effective relaxation time may be known as:

$$\frac{1}{\tau_{eff}} = \frac{1}{\tau_N} + \frac{1}{\tau_B} \tag{10}$$

Previous studies showed that Néel relaxation is more dominating in the case of particles with smaller sizes, while larger particles relax in liquid medium mainly by a Brownian mechanism [24,25,43,44]. The NP sizes deduced from XRD and TEM for our samples allow us to suppose that the contribution of Néel relaxation is more dominant than that of Brownian relaxation. In order to confirm the contribution of Brownian relaxation in the heat dissipated by NPs, the temperature rise was measured in different carrier liquids as shown in Figure 9. It is expected that Brownian relaxation time in liquid with lower viscosity will decreases as described by Equation (9) and that would induce an increase of heating efficiency. It can be observed from Figure 9, that the sample dispersed in acetone reach magnetic hyperthermia (42 °C), while sample in deionized water does not reach this temperature. The heating efficiency clearly increase for NPs dispersed in acetone which has lower viscosity (0.295 mPa.s) compared to deionized water (0.89 mPa.s). Thus, we can conclude that Brownian relaxation mechanism is also contributing to the heat production.

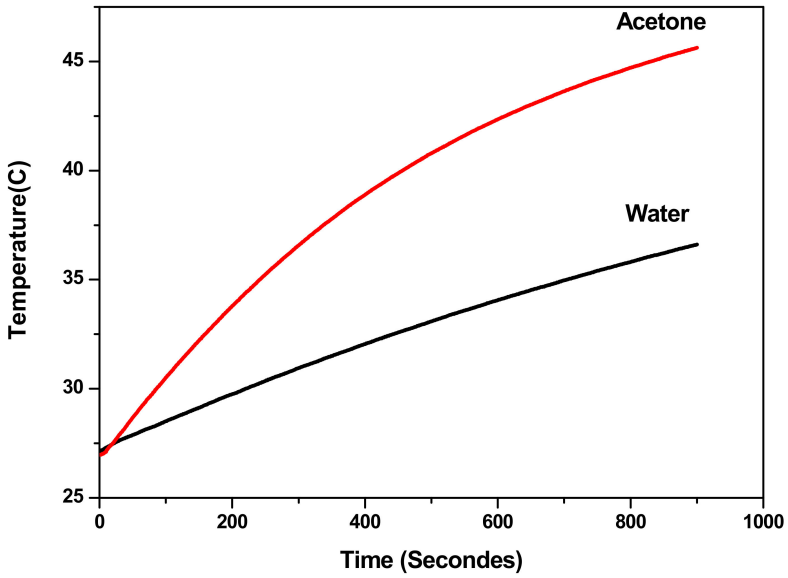


**Figure 9.** Increase in temperature at $H_0$ = 170 Oe and $f$ = 332.8 kHz for γ-$Fe_2O_3$-$TiO_2$ NPs (5 mg/mL) dispersed in deionized water and in acetone.

## 4. Conclusions

In conclusion, a modified sol-gel method was employed to synthesize $\gamma$-$Fe_2O_3$ and $\gamma$-$Fe_2O_3$-$TiO_2$ nanocomposites with small sizes and good uniformity for magnetic hyperthermia applications. Magnetization measurements and heating efficiencies were investigated in detail. The influence of concentration, magnetic field amplitude and carrier liquid on heating efficiency was presented. Our results show that the ILP and SAR values differ slightly between the two samples, but both have high heating efficiency and reach magnetic hyperthermia temperature (42 °C) in relatively short times. While $\gamma$-$Fe_2O_3$ NPs reached magnetic hyperthermia temperatures in 3 min, $\gamma$-$Fe_2O_3$-$TiO_2$ NPs require around 10 min for reaching the same temperature. SAR values indicated that the heating efficiency of the NPs can be tuned by changing the field amplitude or concentration of the NPs. The dependence of SAR values with field amplitude follows linear response theory (LRT). Moreover, the ILP values of 1.57 $nHm^2/kg$ and 0.64 $nHm^2/kg$ obtained for $\gamma$-$Fe_2O_3$ and $\gamma$-$Fe_2O_3$-$TiO_2$, respectively, are in the range reported for commercial ferrofluids ($0.2-3.1$ $nHm^2/kg$), showing their good heating efficiency. The high crystallinity, good SAR and ILP values make these NPs promising candidates for hyperthermia application.

**Author Contributions:** O.M.L., conceptualization, investigation, formal analysis, writing—original draft; N.M., investigation, validation M.A., investigation, validation; S.A., investigation, validation; L.E.M., conceptualization, investigation; A.G., investigation, formal analysis; M.H., investigation; A.A.Y., investigation, formal analysis; K.E.-B., writing—review and editing. All authors have read and agreed to the published version of the manuscript.

**Funding:** This research received no external funding.

**Institutional Review Board Statement:** Not applicable.

**Informed Consent Statement:** Not applicable.

**Acknowledgments:** This research was supported by the Deanship of Scientific Research, Imam Mohammad Ibn Saud Islamic University (IMISU), Saudi Arabia, Grant No. (19-12-12-018).

**Conflicts of Interest:** The authors declare that they have no known competing financial interests or personal relationships that could have appeared to influence the work reported in this paper.

## References

1. El-Boubbou, K. Magnetic iron oxide nanoparticles as drug carriers: Clinical relevance. *Nanomedicine* **2018**, *13*, 953–971. [CrossRef]
2. Wu, W.; Jiang, C.Z.; Roy, V.A.L. Designed synthesis and surface engineering strategies of magnetic iron oxide nanoparticles for biomedical applications. *Nanoscale* **2016**, *8*, 19421–19474. [CrossRef]
3. Khot, V.; Pawar, S. Magnetic Hyperthermia with Magnetic Nanoparticles: A Status Review. *Curr. Top. Med. Chem.* **2014**, *14*, 572–594. [CrossRef]
4. Kossatz, S.; Grandke, J.; Couleaud, P.; Latorre, A.; Aires, A.; Crosbie-Staunton, K.; Ludwig, R.; Dähring, H.; Ettelt, V.; Lazaro-Carrillo, A.; et al. Efficient treatment of breast cancer xenografts with multifunctionalized iron oxide nanoparticles combining magnetic hyperthermia and anti-cancer drug delivery. *Breast Cancer Res.* **2015**, *17*, 66. [CrossRef] [PubMed]
5. Jeon, M.J.; Ahn, C.-H.; Kim, H.; Chung, I.J.; Jung, S.; Kim, Y.-H.; Youn, H.; Chung, J.W. The intratumoral administration of ferucarbotran conjugated with doxorubicin improved therapeutic effect by magnetic hyperthermia combined with pharmacotherapy in a hepatocellular carcinoma model. *J. Exp. Clin. Cancer Res.* **2014**, *33*, 57. [CrossRef] [PubMed]
6. Hayashi, K.; Nakamura, M.; Miki, H.; Ozaki, S.; Abe, M.; Matsumoto, T.; Sakamoto, W.; Yogo, T.; Ishimura, K. Magnetically Responsive Smart Nanoparticles for Cancer Treatment with a Combination of Magnetic Hyperthermia and Remote-Control Drug Release. *Theranostics* **2014**, *4*, 834–844. [CrossRef]
7. Kim, J.; Park, S.; Lee, J.E.; Jin, S.M.; Lee, J.H.; Lee, I.S.; Yang, I.; Kim, J.-S.; Kim, S.K.; Cho, M.-H.; et al. Designed Fabrication of Multifunctional Magnetic Gold Nanoshells and Their Application to Magnetic Resonance Imaging and Photothermal Therapy. *Angew. Chem.* **2006**, *118*, 7918–7922. [CrossRef]
8. Lal, S.; Clare, S.E.; Halas, N. Nanoshell-Enabled Photothermal Cancer Therapy: Impending Clinical Impact. *Acc. Chem. Res.* **2008**, *41*, 1842–1851. [CrossRef]
9. Yang, T.; Tang, Y.; Liu, L.; Lv, X.; Wang, Q.; Ke, H.; Deng, Y.; Yang, H.; Yang, X.; Liu, G.; et al. Size-Dependent $Ag_2S$ Nanodots for Second Near-Infrared Fluorescence/Photoacoustics Imaging and Simultaneous Photothermal Therapy. *ACS Nano* **2017**, *11*, 1848–1857. [CrossRef]
10. Kong, A.; Wang, H.; Li, J.; Shan, Y. Preparation of super paramagnetic crystalline mesoporous $\gamma$-$Fe_2O_3$ with high surface. *Mater. Lett.* **2008**, *62*, 943–945. [CrossRef]

11. Kazeminezhad, I.; Mosivand, S. Phase Transition of Electrooxidized Fe3O4to γ and α-$Fe_2O_3$Nanoparticles Using Sintering Treatment. *Acta Phys. Pol. A* **2014**, *125*, 1210–1214. [CrossRef]
12. Cui, H.; Liu, Y.; Ren, W. Structure switch between α-$Fe_2O_3$, γ-$Fe_2O_3$ and $Fe_3O_4$ during the large scale and low temperature Sol-gel synthesis of nearly monodispersed iron oxide nanoparticles. *Adv. Powder Technol.* **2013**, *24*, 93–97. [CrossRef]
13. El-Boubbou, K. Magnetic iron oxide nanoparticles as drug carriers: Preparation, conjugation and delivery. *Nanomedicine* **2018**, *13*, 929–952. [CrossRef] [PubMed]
14. El-Boubbou, K.; Ali, R.; Al-Zahrani, H.; Trivilegio, T.; Alanazi, A.H.; Khan, A.L.; Boudjelal, M.; AlKushi, A. Preparation of iron oxide mesoporous magnetic microparticles as novel multidrug carriers for synergistic anticancer therapy and deep tumor penetration. *Sci. Rep.* **2019**, *9*, 9481. [CrossRef] [PubMed]
15. Colmenares, J.C.; Ouyang, W.; Ojeda, M.; Kuna, E.; Chernyayeva, O.; Lisovytskiy, D.; De, S.; Luque, R.; Balu, A.M. Mild ultrasound-assisted synthesis of TiO 2 supported on magnetic nanocomposites for selective photo-oxidation of benzyl alcohol. *Appl. Catal. B Environ.* **2016**, *183*, 107–112. [CrossRef]
16. Zhang, Q.; Meng, G.; Wu, J.; Li, D.; Liu, Z. Study on enhanced photocatalytic activity of magnetically recoverable $Fe_3O_4$@C@$TiO_2$ nanocomposites with core–shell nanostructure. *Opt. Mater.* **2015**, *46*, 52–58. [CrossRef]
17. Li, W.; Wu, H. Sodium citrate functionalized reusable Fe3O4@TiO2 photocatalyst for water purification. *Chem. Phys. Lett.* **2017**, *686*, 178–182. [CrossRef]
18. Lendzion-Bieluń, Z.; Wojciechowska, A.; Grzechulska-Damszel, J.; Narkiewicz, U.; Śniadecki, Z.; Idzikowski, B. Effective processes of phenol degradation on Fe3O4–TiO2 nanostructured magnetic photocatalyst. *J. Phys. Chem. Solids* **2019**, *136*, 109178. [CrossRef]
19. Islam, S.; Kusumoto, Y.; Mamun, A.A.; Horie, Y. Photocatalytic and AC magnetic-field induced enhanced cytotoxicity of $Fe_3O_4$–$TiO_2$ core-shell nanocomposites against HeLa cells. *Catal. Commun.* **2011**, *16*, 39–44. [CrossRef]
20. Lu, X.; Li, Y.; Jiang, W.; Huang, Y.; Zhang, W.; Liang, G.; Yang, S. Porous γ-$Fe_2O_3$ microspheres decorated with $TiO_2$ nanocrystals as highly recyclable photocatalysts and potential highly efficient magnetic hyperthermia agents. *J. Mater. Sci. Mater. Electron.* **2018**, *29*, 20856–20865. [CrossRef]
21. Hilger, I.; Frühauf, K.; Andrä, W.; Hiergeist, R.; Hergt, R.; Kaiser, W.A. Heating Potential of Iron Oxides for Therapeutic Purposes in Interventional Radiology. *Acad. Radiol.* **2002**, *9*, 198–202. [CrossRef]
22. Lemine, O.; Madkhali, N.; Hjiri, M.; All, N.A.; Aida, M. Comparative heating efficiency of hematite (α-$Fe_2O_3$) and nickel ferrite nanoparticles for magnetic hyperthermia application. *Ceram. Int.* **2020**, *46*, 28821–28827. [CrossRef]
23. Kita, E.; Hashimoto, S.; Kayano, T.; Minagawa, M.; Yanagihara, H.; Kishimoto, M.; Yamada, K.; Oda, T.; Ohkohchi, N.; Takagi, T.; et al. Heating characteristics of ferromagnetic iron oxide nanoparticles for magnetic hyperthermia. *J. Appl. Phys.* **2010**, *107*, 09B321. [CrossRef]
24. De la Presa, P.; Luengo, Y.; Multigner, M.; Costo, R.; Morales, M.D.P.; Rivero, G.; Hernando, A. Study of Heating Efficiency as a Function of Concentration, Size, and Applied Field in γ-Fe2O3 Nanoparticles. *J. Phys. Chem. C* **2012**, *116*, 25602–25610. [CrossRef]
25. Lemine, O.; Omri, K.; Iglesias, M.; Velasco, V.; Crespo, P.; de la Presa, P.; El Mir, L.; Bouzid, H.; Yousif, A.; Al-Hajry, A. γ-Fe2O3 by Sol-gel with large nanoparticles size for magnetic hyperthermia application. *J. Alloy Compd.* **2014**, *607*, 125–131. [CrossRef]
26. Thorat, N.D.; Lemine, O.; Bohara, R.; Omri, K.; El Mir, L.; Tofail, S.A.M. Superparamagnetic iron oxide nanocargoes for combined cancer thermotherapy and MRI applications. *Phys. Chem. Chem. Phys.* **2016**, *18*, 21331–21339. [CrossRef] [PubMed]
27. Martinez-Boubeta, C.; Simeonidis, K.; Makridis, A.; Angelakeris, M.; Iglesias, O.; Guardia, P.; Cabot, A.; Yedra, L.; Estradé, S.; Peiró, F.; et al. Learning from Nature to Improve the Heat Generation of Iron-Oxide Nanoparticles for Magnetic Hyperthermia Applications. *Sci. Rep.* **2013**, *3*, 1652. [CrossRef]
28. Scherrer, P. Bestimmung der inneren Struktur und der Größe von Kolloidteilchen mittels Röntgenstrahlen. In *Kolloidchemie Ein Lehrbuch*; Springer: Berlin, Germany, 1912; pp. 387–409.
29. Masuda, Y.; Kato, K. Synthesis and phase transformation of $TiO_2$ nano-crystals in aqueous solutions. *J. Ceram. Soc. Jpn.* **2009**, *117*, 373–376. [CrossRef]
30. Morgan, B.J.; Watson, G.W. A Density Functional Theory + U Study of Oxygen Vacancy Formation at the (110), (100), (101), and (001) Surfaces of Rutile TiO2. *J. Phys. Chem. C* **2009**, *113*, 7322–7328. [CrossRef]
31. Larumbe, S.; Gomez-Polo, C.; Pérez-Landazábal, J.; Pastor, J.M. Effect of a $SiO_2$coating on the magnetic properties of Fe3O4nanoparticles. *J. Physics Condens. Matter* **2012**, *24*, 266007. [CrossRef]
32. Chen, Z.; Ma, Y.; Geng, B.; Wang, M.; Sun, X. Photocatalytic performance and magnetic separation of $TiO_2$-functionalized γ-$Fe_2O_3$, Fe, and Fe/$Fe_2O_3$ magnetic particles. *J. Alloy Compd.* **2017**, *700*, 113–121. [CrossRef]
33. Hernando, A.; Vázquez, M.; Kulik, T.; Prados, C. Analysis of the dependence of spin-spin correlations on the thermal treatment of nanocrystalline materials. *Phys. Rev. B* **1995**, *51*, 3581–3586. [CrossRef]
34. Brown, J.W.F. Theory of the Approach to Magnetic Saturation. *Phys. Rev.* **1940**, *58*, 736–743. [CrossRef]
35. Komogortsev, S.; Iskhakov, R. Law of approach to magnetic saturation in nanocrystalline and amorphous ferromagnets with improved transition behavior between power-law regimes. *J. Magn. Magn. Mater.* **2017**, *440*, 213–216. [CrossRef]
36. Craik, D.J. *Magnetic Oxides*; John Wiley & Sons: London, UK; New York, NY, USA, 1975.
37. Lyubutin, I.; Starchikov, S.; Bukreeva, T.; Lysenko, I.; Sulyanov, S.; Korotkov, N.; Rumyantseva, S.; Marchenko, I.; Funtov, K.; Vasiliev, A. In situ synthesis and characterization of magnetic nanoparticles in shells of biodegradable polyelectrolyte microcapsules. *Mater. Sci. Eng. C* **2014**, *45*, 225–233. [CrossRef] [PubMed]

38. Roca, A.G.; Marco, J.F.; Morales, M.D.P.; Serna, C.J. Effect of Nature and Particle Size on Properties of Uniform Magnetite and Maghemite Nanoparticles. *J. Phys. Chem. C* **2007**, *111*, 18577–18584. [CrossRef]
39. Abbasi, A.Z.; Gutiérrez, L.; del Mercato, L.L.; Herranz, F.; Chubykalo-Fesenko, O.; Veintemillas-Verdaguer, S.; Parak, W.J.; Morales, M.P.; González, J.M.; Hernando, A.; et al. Magnetic Capsules for NMR Imaging: Effect of Magnetic Nanoparticles Spatial Distribution and Aggregation. *J. Phys. Chem. C* **2011**, *115*, 6257–6264. [CrossRef]
40. Reyes-Ortega, F.; Fernández, B.L.C.; Delgado, A.V.; Iglesias, G.R. Hyperthermia-Triggered Doxorubicin Release from Polymer-Coated Magnetic Nanorods. *Pharmaceutics* **2019**, *11*, 517. [CrossRef]
41. Hadadian, Y.; Ramos, A.P.; Pavan, T.Z. Role of zinc substitution in magnetic hyperthermia properties of magnetite nanoparticles: Interplay between intrinsic properties and dipolar interactions. *Sci. Rep.* **2019**, *9*, 18048. [CrossRef]
42. Kallumadil, M.; Tada, M.; Nakagawa, T.; Abe, M.; Southern, P.; Pankhurst, Q.A. Suitability of commercial colloids for magnetic hyperthermia. *J. Magn. Magn. Mater.* **2009**, *321*, 1509–1513. [CrossRef]
43. Vallejo-Fernandez, G.; Whear, O.; Roca, A.G.; Hussain, S.; Timmis, J.I.; Patel, V.; Ogrady, K. Mechanisms of hyperthermia in magnetic nanoparticles. *J. Phys. D Appl. Phys.* **2013**, *46*, 312001. [CrossRef]
44. Chung, S.H.; Hoffmann, A.; Bader, S.D.; Liu, C.; Kay, B.K.; Makowski, L.; Chen, L. Biological sensors based on Brownian relaxation of magnetic nanoparticles. *Appl. Phys. Lett.* **2004**, *85*, 2971–2973. [CrossRef]